Materials Research Proceedings 41 (2024) 32-39 https://doi.org/10.21741/9781644903131-4

# Inverse identification of heat source model parameters for laser-powder directed energy deposition of AISI H13 deposit on AISI H11 substrate

BERTRAND Johanna[1,2,a *], ABBES Fazilay[1,b], BONNEFOY Hervé[2,c], FLAN Bruno[2,d] and ABBES Boussad[1,e]

[1] MATIM, Matériaux & Ingénierie Mécanique, Université de Reims Champagne-Ardenne, Reims, FRANCE

[2] Platinium 3D, 08000 Charleville-Mézières, FRANCE

[a]j.bertrand@platinium3d.com, [b]fazilay.abbes@univ-reims.fr, [c]h.bonnefoy@platinium3d.com, [d]b.flan@platinium3d.com, [e]boussad.abbes@univ-reims.fr

**Keywords:** Directed Energy Deposition, Numerical Modeling, Goldak Heat Source, Parameters Identification

**Abstract.** Numerical modeling and simulation are very useful tools for assessing the impact of process parameters and predicting optimized conditions in Laser Directed Energy Deposition (L-DED) processes. Heat source parameters have a great influence on the accuracy of numerical modeling for predicting temperature fields and residual stresses. This paper presents a coupled experimental-numerical procedure to determine the Goldak's heat source model parameters. Graded single-clad tracks were printed with the laser beam power increased continuously at a constant powder feeding rate and scanning speed. Bead widths, heights, and penetration depths were measured at different locations along the deposited track and then used as experimental data for an inverse identification process using the FEA code ABAQUS and the optimizer iSIGHT. The obtained results show that the accuracy of the numerical model is increased with optimized parameters.

## Introduction

Laser Directed Energy Deposition (L-DED) is an economic process to produce three-dimensional complex parts, a very interesting solution for the low-cost repair of damaged high-value components, and for coatings with improved surface properties [1].

To obtain an optimal coating, free of defects such as porosity and cracking [2], it is important to find an appropriate process. According to Thompson et al. [3], the most influencing parameters on the L-DED process are the laser power, the laser scanning speed, the powder feeding rate, the overlap percentage between two single tracks, the dwell time between two layers, the laser spot diameter, and the laser scanning strategy. Testing experimentally so many different parameter combinations can be expensive and time-consuming.

Numerical modeling and simulation are very useful tools for assessing the impact of process parameters and predicting optimized conditions in L-DED processes. In typical residual stress simulations, the thermal part of the process is first simulated, and then the thermal fields are used as input for the mechanical analysis. Indeed, thermal fields play a major role in the quality of L-DED parts. L-DED consists of the deposition of multiple layers, which will be heated up and cooled down as a new layer is deposited. This phenomenon is known as thermal cycling and the resulting thermal history can lead to anisotropic structures [5]. An anisotropic structure can, with use, lead to cracking and thus degrading the part properties [6].

Heat source parameters have a great influence on the accuracy of numerical modeling for predicting temperature fields and residual stresses. The Goldak equivalent heat source (double ellipsoid) is the most widely used heat input model for welding and L-DED simulations [4].

In most cases, Goldak's model parameters are determined from experimentations [7], which consequently leads to errors in simulation as the modeling requirements are more complex and experimental validations have limitations [8]. Thus, the parameters of the heat source model should be optimized to obtain a more accurate melt pool.

In this article, experimental work has been conducted in order to obtain input data for the calibration of the heat source model by printing graded single-clad tracks with the laser beam power increased continuously and keeping constant the powder feeding rate and the scanning speed. To optimize the heat source parameters, the thermal simulation using ABAQUS software was coupled with iSIGHT optimizer. The originality of our work stands in the fact that we do not use thermocouples to adjust our model, but instead, we use experimentally measured bead geometry: width, height, and penetration depth.

**Experimental Methodology**

The substrate used for the experiments was a hot work tool steel bloc (AISI H11) and the deposit was Ferro 55 metal powder (AISI H13) from Voestalpine Böhler. The chemical compositions of these materials are given in Table 1.

*Table 1: Chemical composition of AISI H11 and H13 alloys.*

| Elements | | C | Mn | Si | S | P | Cr | Mo | V | Ni | Cu | Fe |
|---|---|---|---|---|---|---|---|---|---|---|---|---|
| AISI H11 | wt% min | 0.38 | 0.20 | 0.80 | / | / | 4.75 | 1.20 | 0.40 | / | / | / |
| | wt% max | 0.43 | 0.40 | 1.00 | 0.015 | 0.015 | 5.25 | 1.40 | 0.60 | 0.25 | 0.35 | Bal. |
| AISI H13 | wt% | 0.36 | 0.80 | 0.35 | / | / | 7.00 | 2.40 | / | / | / | Bal. |

Graded single-clad tracks were printed by increasing the laser beam power (increase of 50 W each 4 mm) at different constant powder feeding rates and scanning speeds by using a TRUMPF Trulaser Cell 7020 machine and TruDisk 4002 laser system with a Yb:YAG environment and a 1030 nm wavelength. The obtained samples were then cut with an $Al_2O_3$ cutting disk, coated with a phenolic resin, and polished with $Al_2O_3$ and SiC abrasive papers (320, 600, and 1200 grains), then with polishing cloth and diamond polishing paste (9, 6, 3 and 1 µm). After etching with a Nital 4% solution for 1min30s, the samples were observed with a digital microscope Keyence VHX-7000 to measure the height ($H$), width ($W$), and penetration depth ($p$) of the single-clad tracks as illustrated in Fig. 1.

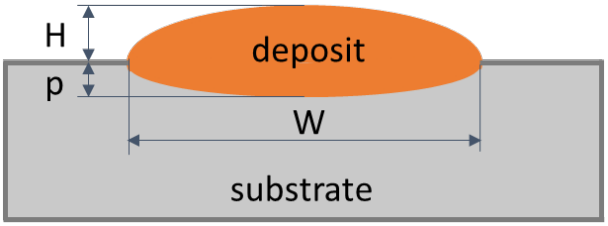


*Fig. 1: Schematic of a cross-section of single-clad track.*

**Thermal Simulation**

The thermal analysis is based on the law of energy conservation and Fourier's law. The equation governing 3D heat transfer is generally stated as:

$$\rho C_p(T)\frac{dT}{dt} = \nabla(\lambda(T)\nabla T) + q_v. \quad (1)$$

where $\lambda(T)$ is a thermal conductivity [W/m/K] and $q_v$ is a laser beam heat source power [W/m$^3$].

Initial condition $T(0) = T_0$ , and boundary conditions considering the convection heat loss and radiation emission heat loss complete Eq. (1) as follows:

$$q_s = -\lambda(T)\frac{\partial T}{\partial n} = h_c(T - T_\infty) + \varepsilon\sigma(T^4 - T_\infty^4). \quad (2)$$

where $h_c$ is the convective coefficient, assumed as $h_c = 25\ [W/m^2/K]$, $\varepsilon$ is the emissivity coefficient, assumed as $\varepsilon = 0.8$, $\sigma$ is the Stefan-Boltzmann constant, and $T_\infty$ is the ambient temperature assumed as $T_\infty = 298\ [K]$.

The Goldak equivalent heat source (double ellipsoid) is considered in this study. Its power density distribution is given by [7]:

$$q_{f/r} = \frac{6\sqrt{3}f_{f/r}}{abc\pi\sqrt{\pi}} Q e^{\frac{-3x^3}{c^2 f/r}} e^{\frac{-3y^2}{a^2}} e^{\frac{-3z^3}{b^2}}. \quad (3)$$

where $a$, $b$, $c_f$, $c_r$ define the axes of the ellipsoidal heat source. $Q$ is the heat source power. $f_{f/r}$ defines the energy flow intensity. Subscript "$f$" represents the region front portion of the melt pool and "$r$" represents the rear region of the melt pool. These parameters will be identified in this study.

The numerical simulation considers temperature dependent thermal conductivity presented in Fig. 2(a) and temperature dependent specific heat presented in Fig. 2(b). The latent heat effect at fusion, which is given in terms of solidus ($T_s$) and liquidus temperatures ($T_l$) and the latent heat ($L_f$), is assumed to be in addition to the specific heat effect. In the simulations, were assumed: $T_s = 1588\ [K]$, $T_l = 1717\ [K]$ and $L_f = 282\ [kJ/kg]$. The density is assumed constant $\rho = 7810\ [kg/m^3]$. In this paper, the same material properties are assumed for AISI H11 and AISI H13.

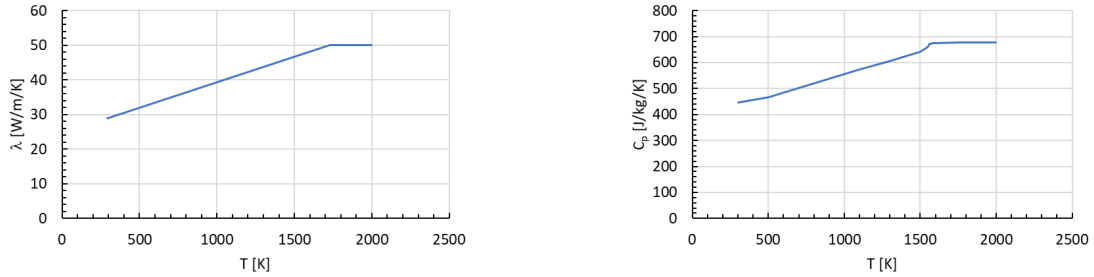


(a) (b)

*Fig. 2: Thermal conductivity (a) and specific heat (b) assumed in simulations.*

The thermal simulation was performed with ABAQUS 2019 software using the built-in features for AM Modeler [9]. Progressive element activation is used to model the deposition of raw material from a moving nozzle. The thermal energy used to heat the bead to the melting point will be applied when the bead is deposited (i.e., activated element). In this study, this energy is distributed over the activated elements assuming a Goldak heat source [10]. The finite element mesh consisted of hexahedral 8-nodes linear thermal elements (type DC3D8) with average edge lengths of 0.5 mm and refined to 0.1 mm in the substrate (on a layer of 1 mm), yielding a model with around 130,000

elements. Figure 3 shows the ABAQUS finite element mesh for the single-clad track. The analysis time increment was locked at Δt = 0.05 [s].

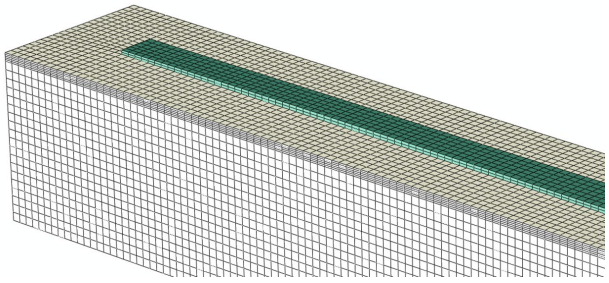

*Fig. 3: Finite element mesh of single-clad track.*

**Inverse Identification Procedure**

Inverse identification method is used to determine the set of the Goldak model parameters that minimize the difference between the calculated values of the thermal model and the corresponding experimental data. The problem is formulated as a least square problem:

Find $P_{opt} \in \mathcal{P}$, such as $\Phi(P_{opt}) = \min_{\mathcal{P}} \Phi(P)$

where:

$$\Phi(P) = \sqrt{\sum_{i=1}^{n} \left(T_i^{sim}(P) - T_i^{exp}\right)^2}. \quad (4)$$

with the constraint:

$$T_{max}^{sim}(P) < T_{ev}. \quad (5)$$

where $\Phi(P)$ is the objective function; $T_i^{sim}(P)$ is the i$^{th}$ calculated temperature; $T_i^{exp}$ is the i$^{th}$ measured temperature; $P$ represents the parameters to be optimized; $n$ is the number of measurements, $\mathcal{P}$ is the constraint space, $T_{max}^{sim}(P)$ is the maximum calculated temperature and $T_{ev}$ is the evaporation temperature assumed as $T_{ev} = 3135\ [K]$ [11].

In this paper, the optimization problem was solved by coupling iSIGHT and ABAQUS. Fig. 4 shows the flow chart of the inverse identification method. In this method, three components were used: i) ABAQUS : performs the numerical thermal simulation using $P$ parameters with similar initial and boundary conditions to experiments and extracts $T_i^{sim}(P)$ and $T_{max}^{sim}(P)$ ; ii) Calculator: calculate $\Phi(P)$ using recorded measurements $T_i^{exp}$ ; iii) Optimization1: adjusts the parameters $P$ by minimizing $\Phi(P)$ with the constraint $T_{max}^{sim}(P) < T_{ev}$. The optimization process stops when the maximum iterations $N$ is reached or when $\Phi(P) < \epsilon$, where $\epsilon = 10^{-6}$ is the global convergence.

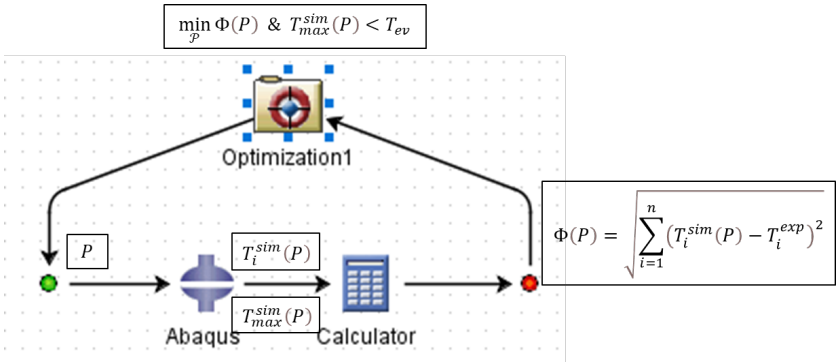


*Fig. 4: Flow chart of the inverse identification method by coupling iSIGHT and ABAQUS.*

**Results and Discussion**

To illustrate the proposed methodology, we have selected a graded bead deposited at a scan speed of $V_s = 0.9$ [m/min] and a powder deposition rate of $F = 25$ [g/min]. The laser beam spot size was measured to be 4 mm in diameter. The laser power was varied from $P = 1450$ to $2550$ [W] (increase of 50 W each 4 mm). Fig. 5 shows the deposited graded bead.


*Fig. 5: Graded bead deposited at $V_s = 0.9\ [m/min]$, $F = 25\ [g/min]$ and $P = 1450\ to\ 2550\ [W]$.*

The obtained sample was then cut along the lines drawn in Fig. 5, coated with a phenolic resin, and polished. After an etching, the cross-sections of cut samples were observed with the digital microscope as shown in Fig. 6. The measured height ($H$), width ($W$) and penetration depth ($p$) of the cuts are given in Table 2.

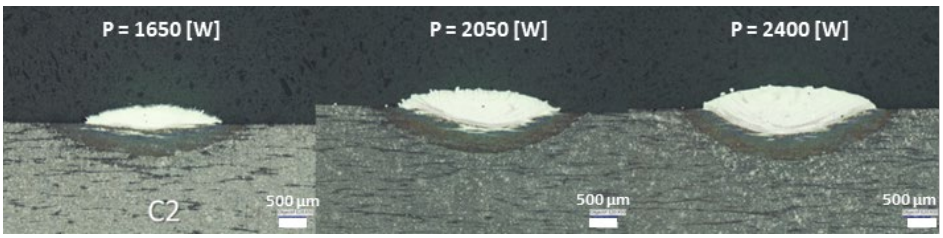


*Fig. 6: Observed cross-sections.*

*Table 2: Measured height, width, and penetration depth of the cross-sections of the graded single-clad track.*

| Cross-section | $P$ [W] | $H$ [mm] | $W$ [mm] | $p$ [mm] |
|---|---|---|---|---|
| 1 | 1650 | 0.338 | 2.330 | 0.098 |
| 2 | 2050 | 0.352 | 3.064 | 0.365 |
| 3 | 2400 | 0.470 | 3.191 | 0.494 |

From the experimental results of the penetration depth ($p$), we have positioned three nodes in the finite element mesh in locations corresponding to the experiment penetration depth to record their temperatures during the simulations. Due to the meshing constraints, the three nodes were

respectively chosen at 0.1 mm, 0.4 mm, and 0.5 mm from the surface of the substrate. The highest temperatures of these nodes during the simulations are extracted automatically from the corresponding ABAQUS output database and used as $T_i^{sim}(P)$ in Eq. (4). The penetration depth corresponds to the melt pool depth [12], where the material reaches its melting temperature assumed as $T_m = 1700$ [K] [13]. The experimental values $T_i^{exp}$ in Eq. (4) were then set to $T_m$ as it is the temperature target in the corresponding node to get the material melted.

Initial model parameters are important for the success of the identification procedure. The double ellipsoid heat source dimensions parameters in Eq. (3) are dependent on experiment cases and are initialized as: $a = W/2$, $b = H + p$, $c_f = W/2$, and $c_r = 2c_f$ [14]. Initial and identified parameters are listed in Table 3.

*Table 3: Initial and identified Goldak's model parameters.*

| Parameters | $P$ [W] | $a$ [mm] | $b$ [mm] | $c_f$ [mm] | $c_r$ [mm] |
|---|---|---|---|---|---|
| Initial | 1650 | 1.165 | 0.436 | 1.165 | 2.330 |
| | 2050 | 1.532 | 0.717 | 1.532 | 3.064 |
| | 2400 | 1.596 | 0.964 | 1.596 | 3.191 |
| Identified | 1650 | 1.165 | 0.498 | 1.040 | 2.301 |
| | 2050 | 1.532 | 0.845 | 1.400 | 3.333 |
| | 2400 | 1.596 | 0.768 | 1.826 | 4.837 |

The calculated temperature histories of three nodes located in the three cross-sections calculated using the double ellipsoid heat source model with the initial and identified parameters are plotted in Fig. 7. The maximum temperatures calculated with the initial parameters are underestimated for the nodes located in the cross-sections 1 and 2 and overestimated for the node located in the cross-section 3 compared to the melting temperature (1700 [K]). However, with the identified parameters, the maximum temperatures for the nodes located in the cross-sections 1 and 2 correspond exactly to the melting temperature, and that for the node located in the cross-section 3 is slightly overestimated without consequences on the final quality of the results given in Fig. 8.

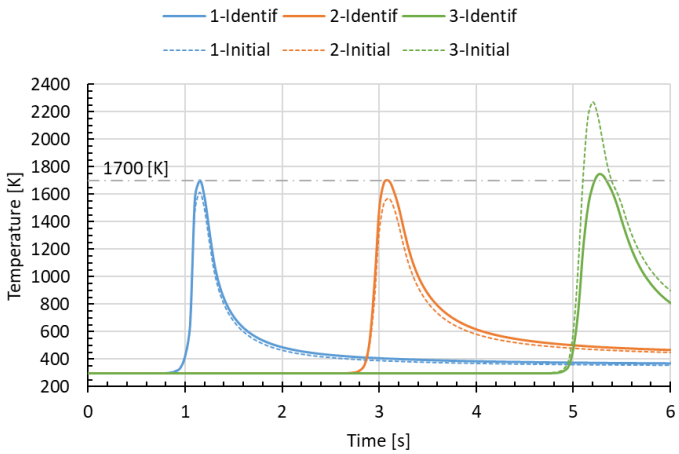


*Fig. 7: Calculated temperature histories of the three nodes located in the three cross-sections.*

Fig. 8 illustrates the temperature distributions on the three cross-sections of the graded single-clad track, which were calculated using the double ellipsoid heat source model with the identified parameters. In all cases, the boundaries of the fusion zone obtained numerically have similar shapes in comparison with the experimental ones. Therefore, numerical values of the bead width, the bead height and the penetrated depth have good agreement with those obtained experimentally.

These results enable this methodology to perform the following analyses based on the identified parameters.

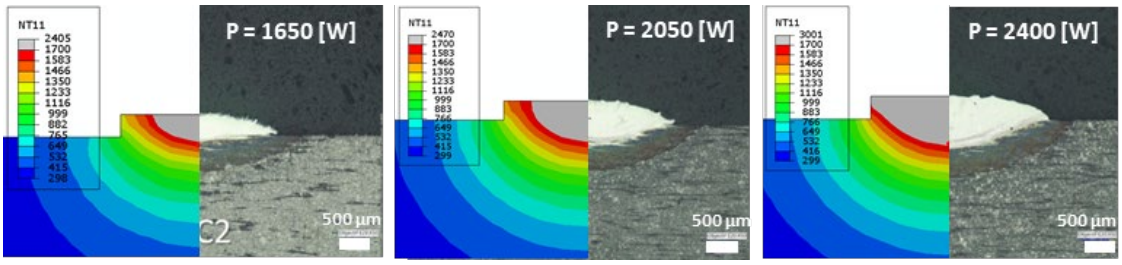


*Fig. 8: Comparison of fusion zone shape, numerically and experimentally obtained for the three cross-sections.*

**Conclusion**

1) Coupling of optimization technique with finite element method, which takes account of experimentally measured bead geometry: width, height, and penetration depth, is important to identify heat source parameters.
2) Printing graded tracks is a low-cost solution for the identification of heat source parameters.
3) The results show that the accuracy of the numerical model is increased with optimized parameters.
4) The proposed identification procedure can be extended to other deposit/substrate couples.

**References**

[1] H. Paydas, A. Mertens, R. Carrus, J. Lecomte-Beckers, J. Tchoufang Tchuindjang, Laser cladding as repair technology for Ti–6Al–4V alloy: Influence of building strategy on microstructure and hardness, Materials and Design 85 (2015) 497–510, http://dx.doi.org/10.1016/j.matdes.2015.07.035

[2] M. Liu, A. Kumar, S. Bukkapatnam, M. Kuttolamadom, A Review of the Anomalies in Directed Energy Deposition (DED) Processes & Potential Solutions - Part Quality & Defects, Procedia Manufacturing 53 (2021) 507–518, https://doi.org/10.1016/j.promfg.2021.06.093

[3] S. M. Thompson, L. Bianc, N. Shamsaei, A. Yadollahi, An overview of Direct Laser Deposition for additive manufacturing; Part I: Transport phenomena, modeling and diagnostics, Additive Manufacturing 8 (2015) 36–62, https://doi.org/10.1016/j.addma.2015.07.001

[4] M. S. Sumanlal, N. S. Sivasubramaniyan, V. M. Joy Varghese, M. Shafeek & D. T. Ananthan, Estimation of heat source model parameters for partial penetration of TIG welding using numerical optimization method, Welding International 37(7) (2023) 400-416, https://doi.org/10.1080/09507116.2023.2242777

[5] N. Kang, X. Lin, M. El Mansori, Q.Z. Wang, J.L. Lu, C. Coddet, W.D. Huang, On the effect of the thermal cycle during the directed energy deposition application to the in-situ production of a Ti-Mo alloy functionally graded structure, Additive Manufacturing 31 (2020) 100911, https://doi.org/10.1016/j.addma.2019.100911

[6] X. Lu, M. Chiumenti, M. Cervera, G. Zhang, X. Lin, Mitigation of residual stresses and microstructure homogenization in directed energy deposition processes, Engineering with Computers 38 (2022) 4771–4790, https://doi.org/10.1007/s00366-021-01563-9

[7] A. Kiran, Y. Li, J. Hodek, M. Brázda, M. Urbánek, and J. Džugan, Heat Source Modeling and Residual Stress Analysis for Metal Directed Energy Deposition Additive Manufacturing, Materials 15(7) (2022) 2545, https://doi.org/10.3390/ma15072545

[8] X. Jia, J. Xu, Z. Liu, et al., A new method to estimate heat source parameters in gas metal arc welding simulation process, Fusion Eng. Des. 89(1) (2014) 40–48, https://doi.org/10.1016/j.fusengdes.2013.11.006

[9] Dassault Systemes, Abaqus Analysis User's Guide 2019, Simulia Inc., Providence, RI, USA (2019).

[10] A. Kiran, J. Hodek, J. Vavřík, M. Urbánek and J. Džugan, Numerical Simulation Development and Computational Optimization for Directed Energy Deposition Additive Manufacturing Process, Materials 13(11) (2020) 2666, https://doi.org/10.3390/ma13112666

[11] "Iron" Breaking Atom. https://www.breakingatom.com/elements/iron (Accessed Jan. 02, 2024).

[12] I. Jeon, L Yang, K. Ryu, & H. Sohn, Online melt pool depth estimation during directed energy deposition using coaxial infrared camera, laser line scanner, and artificial neural network, Additive Manufacturing 47 (2021), 102295, https://doi.org/10.1016/j.addma.2021.102295

[13] "H13 Tool Steel - Chromium Hot-Work Steels" AZO Materials. https://www.azom.com/article.aspx?ArticleID=9107 (Accessed Jan. 02, 2024).

[14] V. Nain, T. Engel, M. Carin, D. Boisselier & L. Seguy, Development of an elongated ellipsoid heat Source model to reduce computation time for directed energy deposition process, Frontiers in Materials 8 (2021), 747389, https://doi.org/10.3389/fmats.2021.747389